Monthly Notices
of the
ROYAL ASTRONOMICAL SOCIETY

MNRAS **489,** 4007–4015 (2019)
Advance Access publication 2019 September 2

doi:10.1093/mnras/stz2425

On the contamination of the global 21-cm signal from polarized foregrounds

Marta Spinelli [1,2]★ Gianni Bernardi[3,4,5] and Mario G. Santos[2,5]

[1]*INAF – Osservatorio Astronomico di Trieste, via G.B. Tiepolo 11, I-34143 Trieste, Italy*
[2]*Department of Physics and Astronomy, University of Western Cape, Cape Town 7535, South Africa*
[3]*INAF – Istituto di Radioastronomia, via Gobetti 101, I-40129 Bologna, Italy*
[4]*Department of Physics and Electronics, Rhodes University, PO Box 94, Grahamstown 6140, South Africa*
[5]*South African Radio Astronomy Observatory, Black River Park, 2 Fir Street, Observatory, Cape Town 7925, South Africa*

Accepted 2019 August 21. Received 2019 August 14; in original form 2019 May 13

ABSTRACT

Global (i.e. sky-averaged) 21-cm signal experiments can measure the evolution of the Universe from the cosmic dawn to the epoch of reionization (EoR). These measurements are challenged by the presence of bright foreground emission that can be separated from the cosmological signal if its spectrum is smooth. This assumption fails in the case of single-polarization antennas as they measure linearly polarized foreground emission – which is inevitably Faraday rotated through the interstellar medium. We investigate the impact of Galactic polarized foregrounds on the extraction of the global 21-cm signal through realistic sky and dipole simulations both in a low-frequency band from 50 to 100 MHz, where a 21-cm absorption profile is expected, and in a higher frequency band (100–200 MHz). We find that the presence of a polarized contaminant with complex frequency structure can bias the amplitude and the shape of the reconstructed signal parameters in both bands. We investigate if polarized foregrounds can explain the unexpected 21-cm cosmic dawn signal recently reported by the Experiment to Detect the Global EoR Signature (EDGES) Collaboration. We find that unaccounted polarized foreground contamination can produce an enhanced and distorted 21-cm absorption trough similar to the anomalous profile reported by Bowman et al., and whose amplitude is in mild tension with the assumed input Gaussian profile (at $\sim 1.5\sigma$ level). Moreover, we note that, under the hypothesis of contamination from polarized foreground, the amplitude of the reconstructed EDGES signal can be overestimated by around 30 per cent, mitigating the requirement for an explanation based on exotic physics.

Key words: polarization – dark ages, reionization, first stars.

1 INTRODUCTION

The 21-cm background arising from the spin–flip transition of neutral hydrogen in the intergalactic medium (IGM) is considered the most promising observable for the cosmic dawn and the subsequent epoch of reionization (EoR; e.g. Pritchard & Loeb 2010). The 21-cm signal is observable as a contrast against the cosmic microwave background (CMB) temperature (Furlanetto, Oh & Briggs 2006). As soon as the first galaxies begin to appear, they produce Lyα photons that couple the excitation temperature of the 21-cm line (spin temperature) to gas kinetic temperature through the Wouthuysen–Field effect (WF; Wouthuysen 1952; Field 1958). As the gravitational collapse progresses, the spin temperature becomes eventually completely coupled to the gas temperature and driven well above the CMB temperature as consequence of the gas heating – most likely by an X-ray background (e.g. Venkatesan, Giroux & Shull 2001; Pritchard & Furlanetto 2007; Mesinger, Ferrara & Spiegel 2013). Observations of 21-cm *fluctuations* from this era of interplay between the Lyα coupling and the X-ray heating will require sensitivities only achievable with the hydrogen EoR (DeBoer et al. 2017) and the upcoming Square Kilometre Array (Koopmans et al. 2015). The measurement of the *global – i.e. sky averaged* – 21-cm signal can be, conversely, achieved by a single-dipole antenna observing for a few tens to a few hundreds of hours (e.g. Shaver et al. 1999; Bernardi, McQuinn & Greenhill 2015; Harker et al. 2016). The 21-cm global signal at the cosmic dawn is expected to be a few hundred mK absorption trough depending on the offset between the WF coupling and the X-ray heating epochs (Pritchard & Loeb 2010). It is sensitive to the formation of the first luminous structures in the universe (e.g. Furlanetto, Oh & Briggs 2006; Mirocha 2014; Mesinger, Greig & Sobacchi 2016), as well

★ E-mail: marta.spinelli@inaf.it

as the thermal history of the IGM (Pritchard & Furlanetto 2007; Mesinger et al. 2013).

At $z \lesssim 10$–15, the sustained galaxy formation produces an ultraviolet radiation background that eventually extinguishes the neutral hydrogen, and therefore the 21-cm signal. The 21-cm signal therefore traces the evolution of the average neutral fraction, essentially timing cosmic reionization.

The Experiment to Detect the Global EoR Signature (EDGES) team has recently reported the detection of a 21-cm absorption profile, centred at 78 MHz, with a 19 MHz width, and an amplitude of 520 mK (Bowman et al. 2018a). This result is more than a factor 2 stronger than standard theoretical predictions and has triggered exotic explanations like interaction with dark matter (e.g. Barkana 2018; Fraser et al. 2018) or axion-induced cooling (e.g. Houston et al. 2018) and a debate on a possible low-frequency excess radio background (e.g. Ewall-Wice et al. 2018; Feng & Holder 2018; Sharma 2018). The unexpected EDGES result is awaiting independent confirmation from the other ongoing global signal experiments. These experiments include the Large-Aperture Experiment to Detect the Dark Ages (LEDA; Price et al. 2018) that constrained at 95 per cent level the amplitude (>-890 mK) and the 1σ width (>6.5 MHz) for a Gaussian model for the trough (Bernardi et al. 2016); the 'Sonda Cosmologica de las Islas para la Deteccion de Hidrogeno Neutro' (SCI-HI; Voytek et al. 2014) that reported a 1 K rms residual in the range 60–88 MHz; the upgraded Shaped Antenna measurement of the background RAdio Spectrum 3 (SARAS 3) that has already provided constraints in the $6 < z < 10$ range (Singh et al. 2017, 2018); the Probing Radio Intensity at high-Z from Marion (PRIZM) experiment (Philip et al. 2019); and the future *Dark Ages Radio Explorer (DARE*; Mirocha, Harker & Burns 2015) is planning to measure the 21-cm global signal. This would also allow to avoid not only terrestrial radio frequency interference, but also ionospheric corruption and solar radio emissions.

The key challenge to measure the 21-cm signal is the subtraction of the bright foreground emission and the consequent control of systematic effects. In presence of smooth-spectrum foregrounds, simulations show that the 21-cm signal can generally be extracted (Nhan, Bradley & Burns 2017; Sathyanarayana Rao et al. 2017; Singh et al. 2017, 2018; Tauscher et al. 2018), particularly using Bayesian techniques (e.g. Harker et al. 2012; Bernardi et al. 2015, 2016; Monsalve et al. 2017, 2018, 2019). This strategy has been employed by Bowman et al. (2018a) too, although their unusual findings have drawn the attention to their foreground modelling and separation method. Hills et al. (2018) have, for example, re-examined the EDGES data and questioned their detection pointing out that the extracted foreground model parameters are unphysical. The reanalysis by Singh & Subrahmanyan (2019), enforcing a maximally smooth foreground model, also found evidence for a different 21-cm signal, substantially more in agreement with the standard predictions.

In this work, we investigate the effect that Galactic polarized foreground emission has on the measurement of the 21-cm signal. Polarized foregrounds that are Faraday rotated through the interstellar medium can leak into total intensity because of imperfect calibration and can, therefore, violate the assumption of smooth spectrum foregrounds. This effect is an active subject of study for interferometric observations (e.g. Bernardi et al. 2010; Jelić et al. 2010; Moore et al. 2013; Martinot et al. 2018), but the case of global signal experiments has received very little attention so far (Switzer & Liu 2014), in particular after the reported detection of the 21-cm signal from the cosmic dawn.

This paper is organized as follow. In Section 2, we describe the contamination from polarized foregrounds in observations carried out with single-dipole antennas and outline the details of our simulations. In Section 3, we describe the extraction of the 21-cm global signal from the simulated spectra, and we conclude in Section 4.

2 SIMULATIONS OF GLOBAL SIGNAL OBSERVATIONS

An individual antenna provides a measurement of the beam-averaged sky brightness temperature $T(\hat{\boldsymbol{r}}_0, \nu, t)$ at the time t and direction $\hat{\boldsymbol{r}}_0$ (e.g. Bernardi et al. 2015):

$$T(\hat{\boldsymbol{r}}_0, \nu, t) = \frac{\int_\Omega A(\hat{\boldsymbol{r}}', \nu)\, T_{\rm sky}(\hat{\boldsymbol{r}}', \nu, t)\, \mathrm{d}\hat{\boldsymbol{r}}'}{\int_\Omega A(\hat{\boldsymbol{r}}', \nu)\, \mathrm{d}\hat{\boldsymbol{r}}'} + T_{\rm N}(\nu, t), \tag{1}$$

where $T_{\rm sky}$ is the sky brightness temperature, A the antenna gain pattern, and $T_{\rm N}$ the instrumental noise. As the sky drifts over the dipole, the sky brightness changes with time, whereas the dipole pattern does not.

A single-polarization antenna inevitably measures polarized emission from the sky. If we call $\boldsymbol{s}$ the intrinsic sky brightness distribution towards a line of sight $\hat{\boldsymbol{r}}$ at the frequency ν in terms of the usual Stokes parameters $\boldsymbol{s} = (I, Q, U, V)^{\rm T}$, the brightness observed by two orthogonal receptors $\boldsymbol{e} = (E_{xx}, E_{xy}, E_{yx}, E_{yy})^{\rm T}$ can be written as (e.g. Ord et al. 2010; Nunhokee et al. 2017)

$$\boldsymbol{e}(\hat{\boldsymbol{r}}, \nu) = \left[\mathbf{J}(\hat{\boldsymbol{r}}, \nu) \otimes \mathbf{J}^*(\hat{\boldsymbol{r}}, \nu)\right] \mathbf{S}\, \boldsymbol{s}(\hat{\boldsymbol{r}}, \nu), \tag{2}$$

where $\mathbf{J}$ is the 2×2 Jones matrix representing the polarized receptor response (i.e. the polarized dipole gain pattern), $\otimes$ is the outer product operator, * denotes the complex conjugate, and $\mathbf{S}$ is the matrix that relates the Stokes parameters to the orthogonal $x-y$ linear feed frame:

$$\mathbf{S} = \frac{1}{2}\begin{pmatrix} 1 & 1 & 0 & 0 \\ 0 & 0 & 1 & i \\ 0 & 0 & 1 & -i \\ 1 & -1 & 0 & 0 \end{pmatrix}.$$

The matrix $\mathbf{A}(\hat{\boldsymbol{r}}, \nu) \equiv \left[\mathbf{J}(\hat{\boldsymbol{r}}, \nu) \otimes \mathbf{J}^*(\hat{\boldsymbol{r}}, \nu)\right]\mathbf{S}$ can be seen as a mixing matrix between the intrinsic and the observed Stokes parameters (e.g. Nunhokee et al. 2017). A single-polarization antenna is described by a Jones matrix of the form

$$\mathbf{J} = \begin{pmatrix} J_x & 0 \\ 0 & 0 \end{pmatrix},$$

and equation (2) leads to

$$E_{xx}(\hat{\boldsymbol{r}}, \nu) = \frac{1}{2} J_x^2(\hat{\boldsymbol{r}}, \nu)\left[I(\hat{\boldsymbol{r}}, \nu, t) + Q(\hat{\boldsymbol{r}}, \nu, t)\right]. \tag{3}$$

Similarly, the orthogonal polarization would be

$$E_{yy}(\hat{\boldsymbol{r}}, \nu) = \frac{1}{2} J_y^2(\hat{\boldsymbol{r}}, \nu)\left[I(\hat{\boldsymbol{r}}, \nu, t) - Q(\hat{\boldsymbol{r}}, \nu, t)\right]. \tag{4}$$

By renaming $A_{x,y} \equiv \frac{1}{2} J_{x,y}^2$, equation (1) can be rewritten explicitly for both polarizations:

$$\begin{aligned} T_{xx}(\hat{\boldsymbol{r}}_0, \nu, t) &= \frac{\int_\Omega E_{xx}(\hat{\boldsymbol{r}}', \nu)\, \mathrm{d}\hat{\boldsymbol{r}}'}{\int_\Omega A_x(\hat{\boldsymbol{r}}', \nu)\, \mathrm{d}\hat{\boldsymbol{r}}'} \\ &= T_{\rm f}(\hat{\boldsymbol{r}}_0, \nu, t) + T_{\rm Q}(\hat{\boldsymbol{r}}_0, \nu, t) + T_{21}(\nu), \\ T_{yy}(\hat{\boldsymbol{r}}_0, \nu, t) &= \frac{\int_\Omega E_{yy}(\hat{\boldsymbol{r}}', \nu)\, \mathrm{d}\hat{\boldsymbol{r}}'}{\int_\Omega A_y(\hat{\boldsymbol{r}}', \nu)\, \mathrm{d}\hat{\boldsymbol{r}}'} \\ &= T_{\rm f}(\hat{\boldsymbol{r}}_0, \nu, t) - T_{\rm Q}(\hat{\boldsymbol{r}}_0, \nu, t) + T_{21}(\nu), \end{aligned} \tag{5}$$

where $T_{\rm f}$ and $T_{\rm Q}$ are the foreground contribution from intensity and polarization, respectively (examined in Sections 2.3 and 2.4), and T_{21} is the contribution to the sky brightness coming from the pristine 21-cm signal that we will discuss further in Section 2.2. Note that we have here neglected the contribution from 21-cm fluctuations as it essentially averages out over large sky areas.

Our goal is to simulate an observed spectrum $\bar{T}_{xx,yy}$ obtained by averaging $T_{xx,\,yy}$ over the observing time – i.e. the data product of a global signal experiment:

$$\bar{T}_{xx}(\nu) = \frac{1}{N_{\rm m}} \sum T_{xx}(t,\,\nu) = \bar{T}_{\rm f}(\nu) + \bar{T}_{\rm Q}(\nu) + T_{21}(\nu),$$
$$\bar{T}_{yy}(\nu) = \frac{1}{N_{\rm m}} \sum T_{yy}(t,\,\nu) = \bar{T}_{\rm f}(\nu) - \bar{T}_{\rm Q}(\nu) + T_{21}(\nu), \quad (6)$$

where $N_{\rm m}$ is the number of measurements over the observation duration.

We consider a dipole located at the Murchison Radio-Astronomy Observatory in Western Australia, where EDGES is located, and that observes the 0 < local sidereal time (LST) < 8 h range with a 1 min cadence. We assume that the noise $T_{\rm N}$ is given by the radiometer equation: it is uncorrelated in frequency and time, and, for each frequency channel, follows a Gaussian distribution with standard deviation:

$$\sigma^{\rm N}_{xx,yy}(\nu) = \frac{\bar{T}_{xx,yy}(\nu)}{\sqrt{\Delta t\,\Delta\nu}}, \quad (7)$$

where we consider a $\Delta\nu = 1$ MHz channel width and a $\Delta t = 400$ h of total integration time. Like EDGES, we consider two separate bands, one covering the low frequency (LF) 50–100 MHz range, and the second covering the higher frequency (HF) 100–200 MHz range.

2.1 Antenna beam model

We used the analytic beam model of the Long Wavelength Array dipole (Taylor et al. 2012; Ellingson et al. 2013; Bernardi et al. 2015) in the LF band:

$$A(\theta,\,\phi,\,\nu) = \sqrt{[p_{\rm E}(\theta,\,\nu)\cos\phi]^2 + [p_{\rm H}(\theta,\,\nu)\sin\phi]^2},$$

where E and H are the two orthogonal polarizations of the dipole and

$$p_i(\nu,\,\theta) = \left[1 - \left(\frac{\theta}{\pi/2}\right)^{\alpha_i(\nu)}\right](\cos\theta)^{\beta_i(\nu)} + \gamma_i(\nu)\left(\frac{\theta}{\pi/2}\right)(\cos\theta)^{\delta_i(\nu)}, \quad (8)$$

where i = E, H. For the coefficient $[\alpha_i,\,\beta_i,\,\gamma_i,\,\delta_i]$ we use the values tabulated in Dowell (2011) and interpolate them in the 50–90 MHz range. The values of the coefficients are then extrapolated to 100 MHz with a third-order polynomial. Fig. 1 displays the beam model for the east–west (E–W) (xx) orientation at LST = 2 h, at 50 and 100 MHz, respectively. For modelling the north–south (N–S) (yy) orientation we switch the E and H terms.

In the absence of a publicly available beam model in the HF band, we directly scale our 100 MHz model linearly with frequency up to 200 MHz.

2.2 Global signal model

The evolution of 21-cm global signal can be computed from physical model parameters via numerical or semi-analytical simulations (e.g. Mirocha 2014; Mirocha, Harker & Burns 2015; Cohen, Fialkov & Barkana 2016; Cohen et al. 2017; Mirocha, Furlanetto & Sun 2017), however, analytic expressions are useful approximation to be used in the evaluation of likelihood functions. In the LF band, the cosmic dawn signal has often been modelled as a Gaussian absorption profile (Bernardi, McQuinn & Greenhill 2015; Presley, Liu & Parsons 2015; Bernardi et al. 2016; Monsalve et al. 2017):

$$T^{\rm LF}_{21,{\rm G}}(\nu) = A_{21}\,{\rm e}^{-\frac{(\nu-\nu_{21})^2}{2\sigma^2_{21}}}, \quad (9)$$

where A_{21}, ν_{21}, and σ_{21} are the amplitude, peak position, and standard deviation of the 21-cm trough, respectively. We consider this our fiducial model for the LF band. We also include the case of a flattened Gaussian profile adopted in the EDGES analysis (Bowman

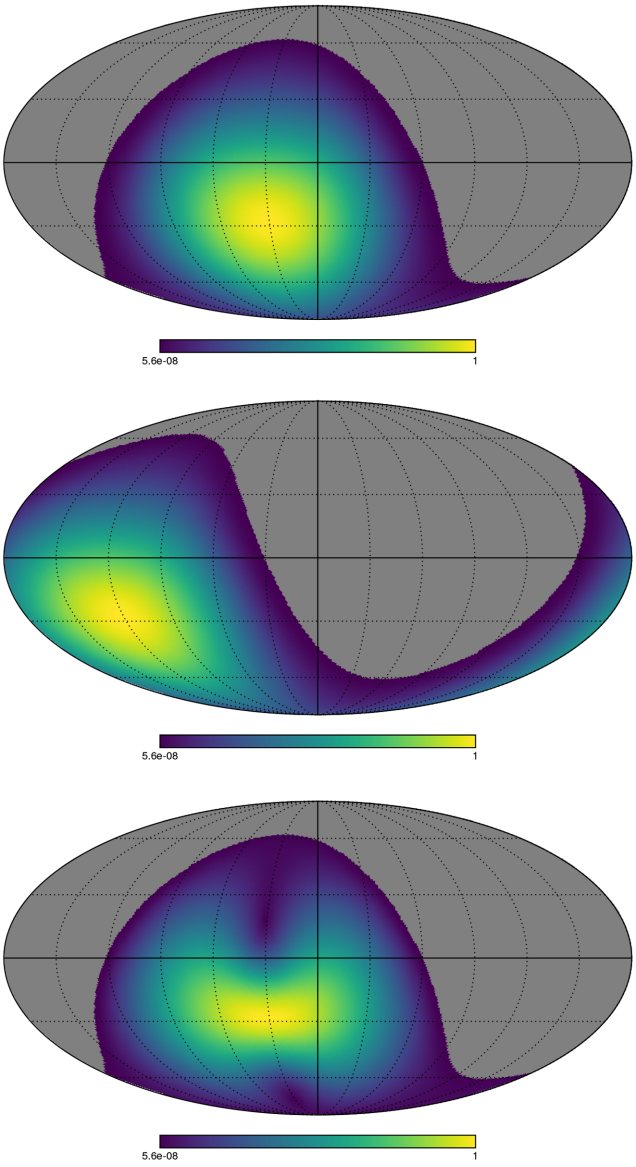

Figure 1. East–west (E–W) (xx) dipole beam model at 50 MHz for local sidereal time (LST) = 2 h (top panel) and LST = 8 h (middle panel). The bottom panel shows instead the 100 MHz beam again for LST = 2 h.

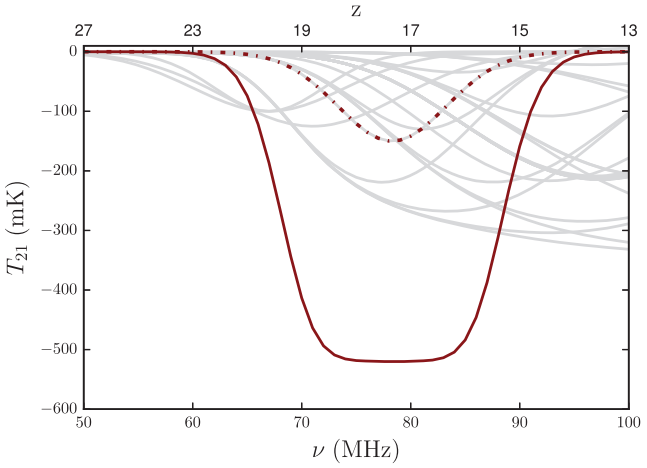

Figure 2. Our fiducial Gaussian input model (dot–dashed red line) and the flattened Gaussian model best fit of the EDGES data (Bowman et al. 2018a, solid red line), compared with the global signal profiles obtained with SIMFAST21 (Santos et al. 2010) varying the physical input parameters (solid grey lines).

et al. 2018a):

$$T_{21,\mathrm{fG}}^{\mathrm{LF}}(\nu) = A_{21}\left(\frac{1-\mathrm{e}^{-\tau \mathrm{e}^{B}}}{1-\mathrm{e}^{-\tau}}\right), \tag{10}$$

where

$$B = \frac{4(\nu-\nu_{21})^2}{w^2}\log\left[-\frac{1}{\tau}\log\left(\frac{1+\mathrm{e}^{-\tau}}{2}\right)\right]. \tag{11}$$

The free parameters here are the amplitude A_{21}, the central frequency ν_{21}, the full width at half-maximum w, and the flattening factor τ. Theoretical simulations that include standard physics predict a wide range of different global 21-cm signals (see e.g. Fig. 2). The largest theoretical unknown is related to the nature of the first luminous sources (e.g. Furlanetto et al. 2006; Mirocha 2014) and the efficiency of the IGM heating (Pritchard & Furlanetto 2007; Fialkov & Loeb 2013; Mesinger et al. 2013; Cohen et al. 2017). As shown in Fig. 2, not even models that predict the brightest absorption profiles are a close match to the EDGES result. Our fiducial model in the HF band is a hyperbolic tangent, a widely used parametrization of the global signal during EoR (e.g. Pritchard & Loeb 2010; Monsalve et al. 2017):

$$T_{21}^{\mathrm{HF}}(z) = a_{21}x_{\mathrm{H\,I}}(z)\sqrt{\frac{1+z}{10}}, \tag{12}$$

where $a_{21} = 28$ mK (Madau, Meiksin & Rees 1997; Furlanetto, Oh & Briggs 2006) and

$$x_{\mathrm{H\,I}}(z) = \frac{1}{2}\left[\tanh\left(\frac{z-z_{\mathrm{r}}}{\Delta z}\right)+1\right]. \tag{13}$$

The free parameters are here the redshift z_{r} at which $x_{\mathrm{H\,I}} = 0.5$ and the reionization duration, $\Delta z = (\mathrm{d}x_{\mathrm{H\,I}}/\mathrm{d}z)^{-1}|_{x_{\mathrm{H\,I}}=0.5}$.

2.3 Total intensity foreground model

A total intensity all-sky map could be used to evaluate the observed foreground spectrum $\bar{T}_{\mathrm{f}}$ via equations (5) and (6) as it was done, for example, in Bernardi et al. (2015). Rather than repeating a similar simulation, we directly calculated the total intensity foreground spectrum averaged over the duration of the observations, i.e. the left-hand side of equation (6).

Table 1. Coefficients of the Galactic synchrotron spectrum model (from Bernardi et al. 2015).

$\log_{10}(p_0/\mathrm{K})$	p_1	p_2	p_3	p_4
3.58	−2.60	0.01	0.06	0.25

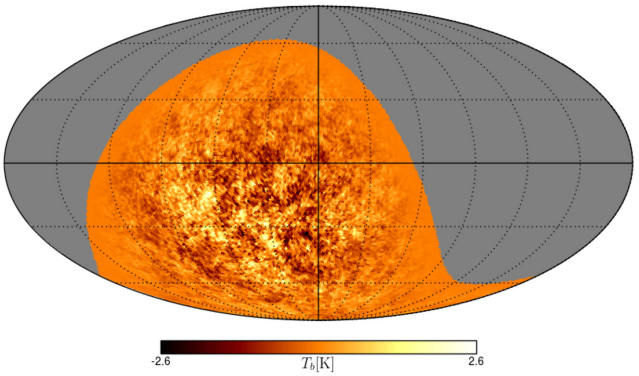

Figure 3. Example of a simulated Stokes Q map at 80 MHz after the dipole beam pattern is applied.

The Galactic foreground spectrum has often been modelled as a Nth-order log-polynomial (e.g. Bowman & Rogers 2010; Pritchard & Loeb 2010; Harker et al. 2012; Bernardi et al. 2015, 2016; Presley et al. 2015):

$$\log_{10}\bar{T}_{\mathrm{f}}(\nu) = \sum_{n=1}^{N} p_{n-1}\left[\log_{10}\frac{\nu}{\nu_0}\right]^{(n-1)}, \tag{14}$$

with $\nu_0 = 60$ MHz. In earlier works, the foreground spectrum was modelled with few frequency components (e.g. Pritchard & Loeb 2010), but more recent simulations suggest that, due to the coupling between the antenna beam pattern and the sky brightness, N should likely take higher values (Harker et al. 2012; Bernardi et al. 2015, 2016; Mozdzen et al. 2016). Here we used the best-fitting coefficients derived from simulations in Bernardi et al. (2015), with a $N = 4$ log-polynomial (see Table 1), a case similar to the analysis in Bowman et al. (2018a).

2.4 Polarized foreground model

We use the simulations in Spinelli, Bernardi & Santos (2018, hereafter S18) to produce Stokes Q and U full sky maps in the 50–200 MHz range with 1 MHz frequency resolution. The S18 full sky simulations are based on the interferometric observations that sample up to degree angular scales (Bernardi et al. 2013) that were extrapolated up to tens of degrees scales, relevant for global signal observations. They are constructed from rotation measure synthesis data that measure the polarized intensity as a function of Faraday depth ϕ (Burn 1966; Brentjens & de Bruyn 2005). Fig. 3 displays an example of a Stokes Q map observed through the dipole beam (equation 5). We generate two sets of polarized foreground spectra $\bar{T}_Q(\nu)$.

(i) One that uses S18 simulations with the full range of ϕ values from the data. We will refer to this simulation as the 'all ϕ' case.

(ii) A second one where high values of the Faraday depth ϕ ($\phi >$ 5 rad m^{-2}) are excluded from the S18 simulations. The motivation behind this choice is to create a more realistic model in the LF band. Observations indicate that Galactic polarized emission has a more

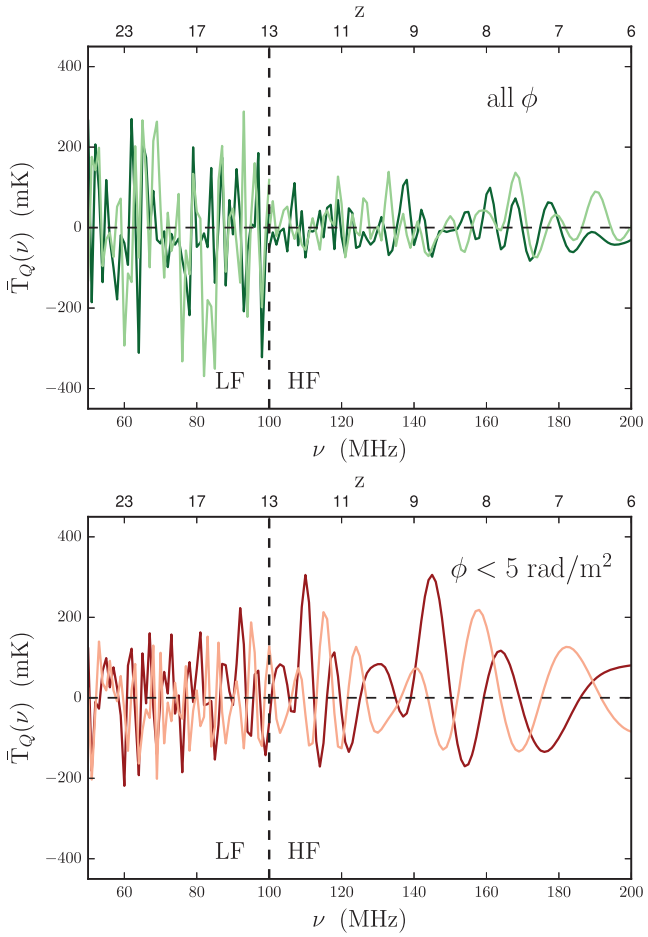

Figure 4. Top panel: simulated polarized foreground spectra $\bar{T}_Q(\nu)$ (equation 1) integrated over the local sidereal time (LST) range. Light and dark green solid lines correspond to two different realizations of the 'all ϕ' simulations. The vertical dashed line divides the LF band from the HF one. Bottom panel: same as the top panel but with light and dark red lines corresponding to two different realizations of the 'low ϕ' (i.e. $\phi < 5$ rad m^{-2}) simulations.

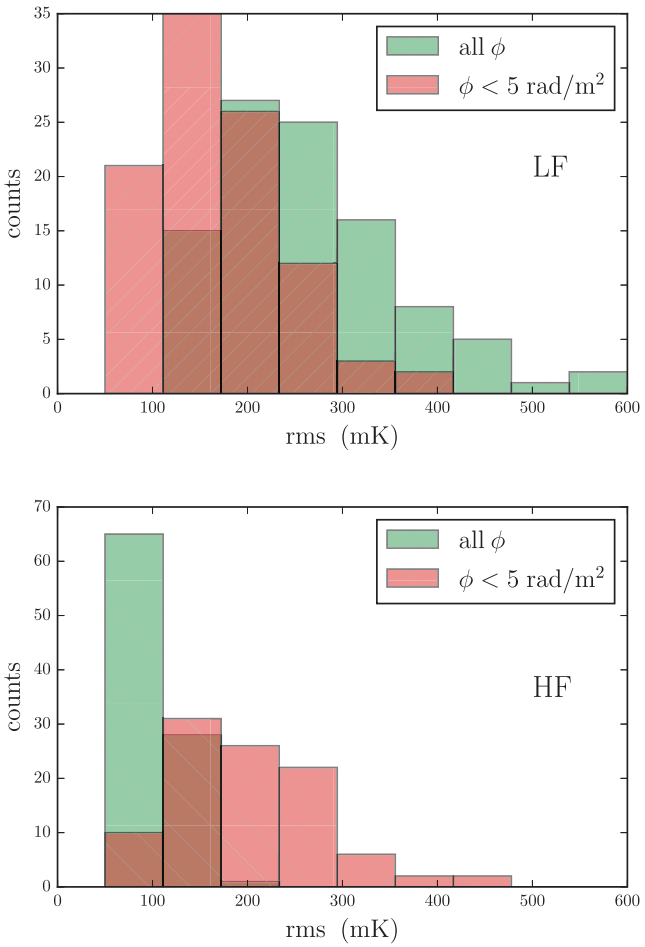

Figure 5. Top panel: distribution of the polarized spectrum rms calculated in the LF band from 100 realizations for both the 'all ϕ' (in green) and the 'low ϕ' (i.e. $\phi < 5$ rad m^{-2}) simulations (in red). Bottom panel: same as the top panel but for the HF band.

local origin with decreasing frequency (e.g. Haverkorn, Katgert & de Bruyn 2004; Bernardi et al. 2009; Lenc et al. 2016) and, therefore, very little emission at high Faraday depth values. We will refer to this simulation as the 'low ϕ' case (i.e. $\phi < 5$ rad m^{-2}).

The combination of the integrated effect of the beam and the complex Faraday structure results in spectra like the one shown in Fig. 4, where two representative realizations of both sets of simulations for both the LF and HF band are displayed. In the LF band, the 'all ϕ' simulation leads to a considerable more complex spectral structure and higher contamination with respect to the 'low ϕ' case – as expected. The oscillatory behaviour becomes smoother in the HF band for both cases but, although there are fewer peaks, the contamination is more prominent for the 'low ϕ' case.

We calculated the rms of $\bar{T}_Q(\nu)$ for every realization and plot its distribution in Fig. 5. In the LF band, the average rms contamination is ∼250 mK for the 'all ϕ' case, with an extended tail at high values. The average contamination is smaller in the other case, peaking around ∼150 mK. The situation is opposite in the HF band, where the 'all ϕ' simulation has an average rms contamination smaller than ∼100 mK, whereas the 'low ϕ' case spans a much broader range of values with an extended tail up to ∼400 mK. It is worth noticing that the estimated rms contamination is generally higher or comparable with the expected 21-cm signal, although our simulations likely represent a worst-case scenario as they do not account for time of frequency-dependent depolarization effects. Time variable electron density and variations of the magnetic fields across the field of view both depolarize the signal when integrated over long observations. Simulations by Martinot et al. (2018) estimated the depolarization to be a factor of 4 or more when averaging over days and over a ∼10° sky patch. The effect can be even more pronounced for global signal observations. Frequency-dependent polarization arises when emitting clouds are Faraday thick, i.e. synchrotron emission and Faraday rotation are colocated within the cloud (Burn 1966; Tribble 1992). Its magnitude depends upon the detailed physics of the interstellar medium and therefore it is fairly uncertain. We note, however, that polarized fluctuations at 350 MHz are of the order of a few Kelvin that extrapolated at 150 MHz with a fiducial spectral index $\beta = -2.6$ would lead to polarized signals at the level of a few tens of Kelvin. Polarized fluctuations remain at the 10–20 K level in the 150–200 MHz range (e.g. Bernardi et al. 2013; Lenc et al. 2016), implying that part of the emission happens in Faraday thick regions and it is Faraday depolarized at low frequencies. In order to empirically account for these effects, we also considered a more optimistic case where the magnitude of the polarized spectrum is reduced to a 10 per cent of the current simulation value. This choice

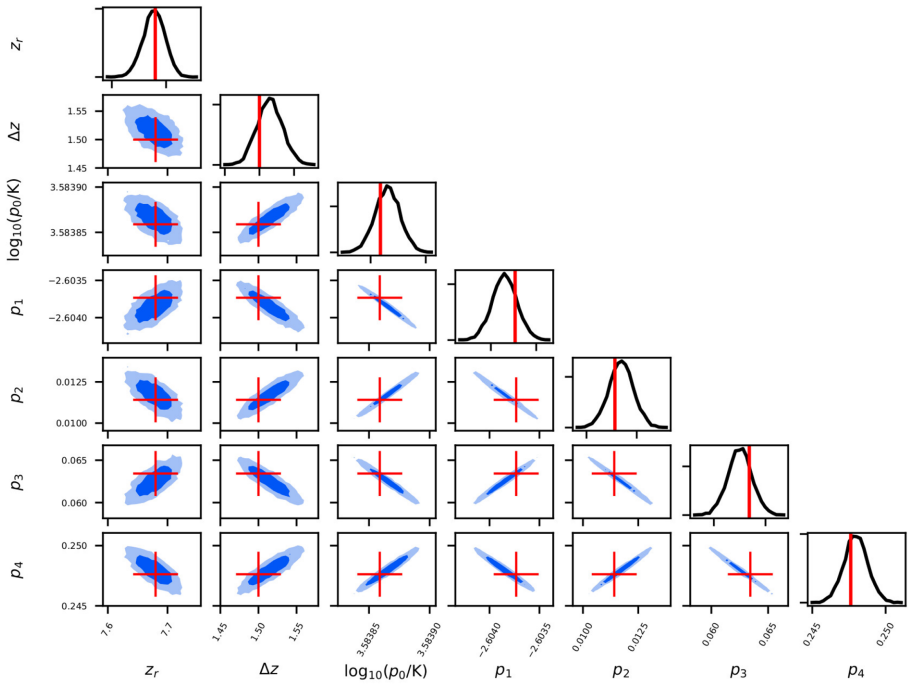

Figure 6. Marginalized two-dimensional posterior distributions of the global 21-cm signal in the HF band and only the total intensity foreground parameters, without including any contamination from polarized foregrounds. Contours are shown at 1σ and 2σ, respectively, whereas the red crosses indicate the input parameter values. The agreement shows that the reconstruction is unbiased in the case of smooth foregrounds.

is in qualitative agreement with the magnitude of the residual rms in the Bowman et al. (2018a) observations.

The final product of our simulations is a sky spectrum $\bar{T}(\nu)$ that is the sum of four different components: a 21-cm signal $T_{21}(\nu)$ as described in Section 2.2; a total intensity foreground spectrum that follows a Nth-order log polynomial (see Section 2.3); a polarized foreground spectrum $\bar{T}_Q(\nu)$ (Section 2.4); and a noise realization drawn from a Gaussian distribution (equation 7). The next section describes the extraction of the 21-cm signal from the simulated spectra.

3 SIGNAL EXTRACTION

In order to extract the global 21-cm signal from the simulated spectra we use the HIBAYES code (Bernardi et al. 2016; Zwart, Price & Bernardi 2016), a fully Bayesian framework where the posterior probability distribution is explored through the MULTINEST sampler (Feroz & Hobson 2008; Feroz, Hobson & Bridges 2009) using a Message Passing Interface (MPI)-enabled PYTHON wrapper (Buchner et al. 2014). The likelihood $\mathcal{L}_i$ of the simulated spectra can be written as

$$\mathcal{L}(\bar{T}(\nu_i)|\boldsymbol{\theta}) = \frac{1}{\sqrt{2\pi\sigma_{\rm N}^2(\nu_i)}} \exp\left(-\frac{(\bar{T}(\nu_i) - T_{\rm m}(\nu_i,\boldsymbol{\theta}))^2}{2\sigma_{\rm N}^2(\nu_i)}\right), \quad (15)$$

where $\boldsymbol{\theta}$ is the vector of model parameters, $\sigma_{\rm N}$ is the noise standard deviation (equation 7), and $T_{\rm m}(\nu_i,\boldsymbol{\theta})$ is the model spectrum. We impose uniform prior on the signal parameters assuming the signal is present within the observed band. For the HF band this translates into a limit for the middle point of reionization, i.e. $6 < z_{\rm r} < 13$, and for the reionization duration, i.e. $0 < \Delta z < 13$. In the LF band we set the priors to be $40 < \nu_{21} < 100$ MHz, $0 < \sigma_{21} < 50$ MHz, and, solely to reduce the computational load, $-1 < A_{21} < 0$ K. We use uniform priors for all the foreground parameters but for the $p_{n=0}$ case where we use a flat logarithmic prior.

As a test case similar to the simulations carried out in Harker et al. (2012) and Bernardi et al. (2016), we show in Fig. 6, the recovery of the global 21-cm signal in the HF band (equation 12) with $z_{\rm r} = 7.68$ and $\Delta z = 1.50$, in agreement with Planck Collaboration XIII (2016) and in the analysis by Monsalve et al. (2017).

We then add the simulated polarized spectrum to the total intensity one. We simulate both equations (3) and (4), i.e. both the xx and yy polarization. We extract the 21-cm signal from three different simulated cases.

(i) The 21-cm signal in the LF band is a flattened Gaussian with $A_{21} = -520$ mK, $\nu_{21} = 78.3$ MHz, $w = 20.7$ MHz, and the flattening parameter $\tau = 7$, i.e. the EDGES best-fitting model (Bowman et al. 2018a). The model spectrum used in the likelihood function is $T_{\rm m} = \bar{T}_{\rm f} + T_{21,\rm fG}^{\rm LF}$.

We generated 50 different realizations of the polarized foreground spectra and reconstruct $T_{21}(\nu)$ from the best-fitting parameters of the posterior distribution for each of them. We discard the cases where our reconstructed signal is localized at high frequency (>90 MHz) as the presence of an absorption signal in the EDGES High-Band has been excluded at $\gtrsim 2\sigma$ (Monsalve et al. 2017). After this selection, we are left with ∼80 per cent of the total number of simulations. The mean and variance of the reconstructed 21-cm profiles are computed separately for the xx and yy polarizations and displayed as a shaded region in Fig. 7.

Because of the unmodelled polarized component, the residual spectra obtained after subtracting the best-fitting model, have relatively high rms values, at the 90–150 mK level. In the 'all ϕ' case, the presence of an unmodelled polarized foreground introduces a bias in both the amplitude and the width of the reconstructed signal. In the 'low ϕ' case the bias is mainly in the amplitude although the

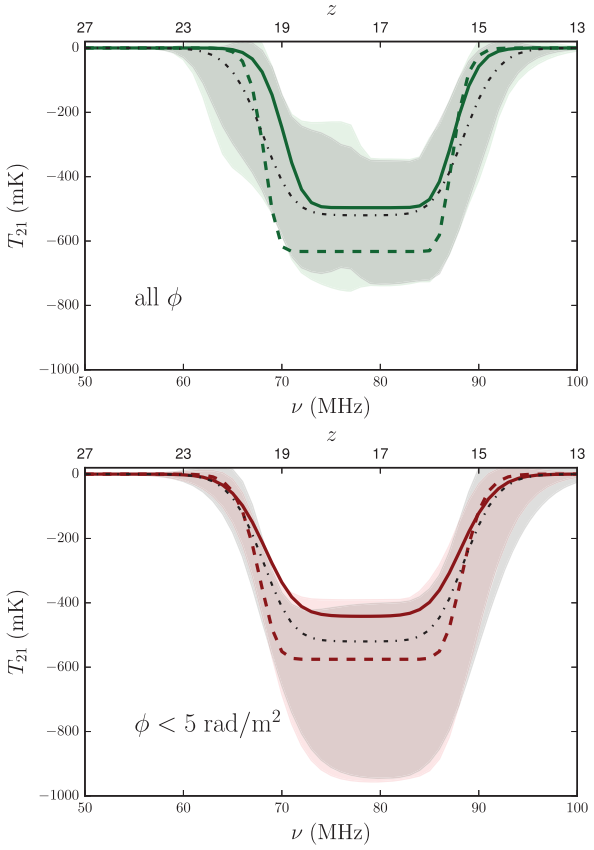

Figure 7. The black dotted–dashed line in both panels is the input signal: the best-fitting flattened Gaussian from Bowman et al. (2018a). Top panel: reconstructed $T_{21,\,\mathrm{fG}}$ signal in the case of the 'all ϕ' simulations, in the LF, from the Bayesian analysis described in the text. The solid (dashed) green line shows one of the reconstructed $T_{21,\,\mathrm{fG}}$ signals for the *xx* (*yy*) polarization The green (grey) shaded area is the 1σ region around the mean for the *xx* (*yy*) polarization (see text for details). Bottom panel: same as top panel but for the 'low ϕ' (i.e. $\phi < 5$ rad m^{-2}) simulations. The red (grey) shaded area is the 1σ region around the mean for the *xx* (*yy*) polarization, and the solid (dashed) red line shows one of the reconstructed signal for both *xx* (*yy*) case.

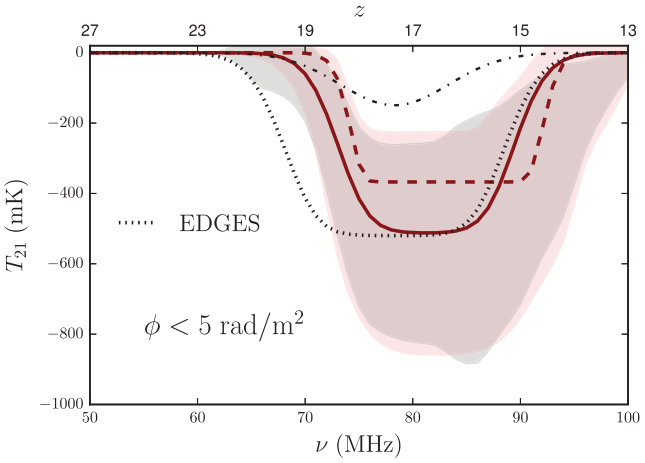

Figure 8. Reconstructed $T_{21,\,\mathrm{fG}}$ signal. Note that the input signal is the fiducial Gaussian model (black dotted–dashed). The solid (dashed) red line shows one of the reconstructed $T_{21,\,\mathrm{fG}}$ signals for the *xx* (*yy*) polarization. The red (grey) shaded area is the 1σ region around the mean for the *xx* (*yy*) polarization (see text for details). For comparison we also show the EDGES best fit (dotted line).

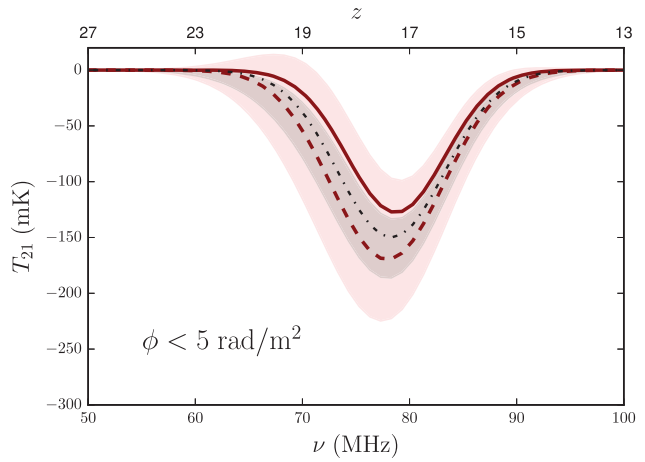

Figure 9. The black dotted–dashed line is the Gaussian fiducial input signal in the LF band. We show here reconstructed $T_{21,\,\mathrm{G}}$ signal considering the 'low ϕ' (i.e. $\phi < 5$ rad m^{-2}) case with signal magnitude reduced to the 10 per cent of the reference simulation – see text for details. The red (grey) shaded area is the 1σ region around the mean for the *xx* (*yy*) polarization. The solid (dashed) red line shows one of the reconstructed $T_{21,\,\mathrm{G}}$ signal for the *xx* (*yy*) polarization.

reconstructed flattening parameter is often different between the two polarization cases. Fig. 7 shows that the reconstructed amplitude is up to ∼40 per cent different than the input signal, at 1σ confidence level.

(ii) The 21-cm signal in the LF band is a Gaussian with $A_{21} = -150$ mK, $\nu_{21} = 78.3$ MHz, and $\sigma_{21} = 5$ MHz, i.e. the fiducial signal expected from standard theoretical models (e.g. Pritchard & Loeb 2010; Mirocha et al. 2015). We first model this signal using a flattened Gaussian shape in order to test whether or not the unusual shape reported by Bowman et al. (2018b) can be due to the contamination from polarized foregrounds, i.e. $T_{\mathrm{m}} = \bar{T}_{\mathrm{f}} + T^{\mathrm{LF}}_{21,\mathrm{fG}}$.

We find that the polarized contamination is significant and, in many realizations, prevents the convergence within the prior range or leads to reconstructed profiles with a high-frequency trough that are, again, discarded from the analysis. Note that we retain a reconstructed profile if these criteria are satisfied by both polarizations. In the 'all-ϕ' case, we discard almost all realizations, concluding that the level of contamination of the simulation is too high for this scenario. On the contrary, using the 'low ϕ' simulations, it is possible to select a meaningful subsample of realizations. Indeed, in this case, we retain the reconstructed profile in both polarizations for ∼30 per cent of the cases (Fig. 8). As discussed in Section 2.4, we also consider a more optimistic case with a magnitude of the polarized spectrum reduced to a 10 per cent value of the current simulations. Even at this reduced level of contamination, the reconstruction remains biased in a way similar to what is shown in Fig. 8.

We eventually extract the 21-cm signal using a Gaussian model $T_{\mathrm{m}} = \bar{T}_{\mathrm{f}} + T^{\mathrm{LF}}_{21,\mathrm{G}}$, i.e. the same functional form used for the simulation input. The magnitude of the polarized contamination prevents the extraction of the 21-cm signal in virtually all the simulated cases. We find, instead, convergence for all cases when the contamination is reduced to the 10 per cent level (Fig. 9). The effect of the polarized leakage is, again, a bias similar to the one in Fig. 7.

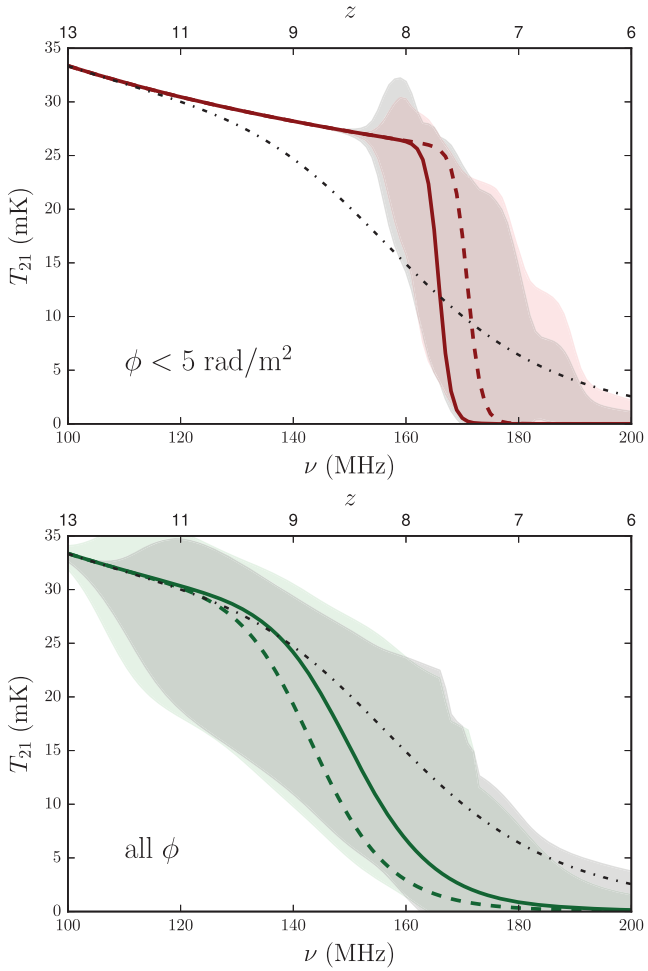

Figure 10. The black dotted–dashed line in both panels is the fiducial input EoR signal. Top panel: reconstructed T_{21} signal in the HF band, in the 'low ϕ' (i.e. $\phi < 5$ rad m^{-2}) case with a 10 per cent reduced magnitude (see text for details). The solid (dashed) red line shows one of the reconstructed $T_{21}^{\rm HF}$ signal for the *xx* (*yy*) polarization. The red (grey) shaded area is the 1σ region around the mean for the *xx* (*yy*) polarization. Bottom panel: same as top panel but for the 'all ϕ' simulations. The green (grey) shaded area is the 1σ region around the mean for the *xx* (*yy*) polarization, and the solid (dashed) green line shows one of the reconstructed signal for the *xx* (*yy*) case.

(iii) The 21-cm signal is the fiducial HF band model (Section 2.2). The contamination derived from our simulations is significantly higher than the 21-cm signal, preventing the convergence of the extraction algorithm to a physically meaningful solution for Δz, the reionization duration. When we consider the case of a 10 per cent contamination, we find that the extraction is possible, although the recovered signal is noticeably biased (Fig. 10). As already noticed in Section 2.4, the bias is stronger in the 'low ϕ' case (up to 10 per cent), where Δz systematically tends to lower values. The bias is still present in the 'all ϕ' case, but less pronounced.

4 DISCUSSION AND CONCLUSIONS

In this paper, we have studied the impact of polarized foregrounds on the measurement of the 21-cm global signal. We simulated realistic observations taken with a zenith-pointing dipole, spanning an 8 h range with a 1 min cadence. Simulations include the all-sky polarized foreground template maps from S18 and a realistic dipole beam in order to generate polarized spectra. We also include a different polarized template where the contamination is reduced to low Faraday depth values, i.e. $\phi < 5$ rad m^{-2}. We simulate two antenna orientations (*xx* and *yy*) separately, using the corresponding beam models. We also consider a more optimistic case where the amplitude is 10 per cent of the template maps in order to empirically account for depolarization effects not included in the S18 model. Total intensity foregrounds are directly modelled through their spectra, as a fourth-order log-polynomial function.

We included three different 21-cm global signal models: a fiducial EoR tanh model in the 100–200 MHz (HF) range, a fiducial Gaussian and a flattened Gaussian (Bowman et al. 2018a) absorption profile in the 50–100 MHz range (LF). We performed a Bayesian extraction of the global 21-cm signal from the simulated spectra.

We draw a few main conclusions from our work. We find that, generally, the contamination from our polarized foreground model has a magnitude and frequency behaviour that prevents the extraction of the 21-cm fiducial signal both in the HF and LF bands. In order to detect the signal, the contamination needs to be fainter: at the $\sim$10 per cent magnitude level, the extraction of the 21-cm signal in both bands is possible, but is significantly biased. In the HF band, the middle point of reionization is biased up to the 10 per cent level and the duration of reionization is poorly recovered, underestimated by a factor up to 10. In the LF band, the bias affects the amplitude of the fiducial cosmic dawn Gaussian signal at the 20 per cent level.

The contamination from polarization leakage can be mitigated by the subtraction of the two orthogonal polarizations observed by a dual polarization antenna. Asymmetries in the beam pattern and errors in the relative calibration of the two polarizations can still, however, introduce polarization contamination at some level. By reducing the magnitude of the polarized signal to the 10 per cent level, we mimic this case too and show that the contamination may not be negligible even in dual polarization observations, in particular for the fiducial EoR model. For example, Monsalve et al. (2017) find a periodic residual signal at the 30 mK level that could be consistent with polarization contamination.

In the light of the detection of the cosmic dawn signal reported by Bowman et al. (2018a), we include their flattened Gaussian absorption model in our simulations. We test a case where the simulation input is the fiducial cosmic dawn Gaussian absorption that we, however, model as a flattened Gaussian profile in the extraction. We find that in this case the signal extraction is possible even at the level of polarized intensity predicted by our simulations, if we consider the 'low ϕ' (i.e. $\phi < 5$ rad m^{-2}) realizations. We find that the polarization contamination tends to introduce a bias in the recovered 21-cm signal, increasing both its amplitude and width for both polarization orientations, leading to a profile similar to what Bowman et al. (2018a) observed. Because of the modelling uncertainties, the bias evidence remains statistically weak, i.e. in tension with the input fiducial Gaussian signal only at the $\sim 1.5\sigma$ level.

In order to exclude the contamination from polarized foregrounds, Bowman et al. (2018a) carried out two measurements where the dipole antenna was rotated by 90°. The best-fitting signal was consistent in both cases, with a 10–20 per cent difference in amplitude (see fig. 2 in Bowman et al. 2018a). We find that the difference between the 21-cm signal extracted from *xx* and *yy* polarization orientations is at a similar level in our simulated cases. This result indicates that measurements with a rotated antenna do not necessarily exclude the polarized contamination and implies that the use of a dual polarization antenna would not automatically remove the problem of polarized foregrounds.

We also simulate the case with a flattened Gaussian profile as both simulation input and model in the extraction. We find that the signal extraction is possible in the 80 per cent of runs for both the 'all ϕ' and the 'low ϕ' (i.e. $\phi < 5$ rad m^{-2}) cases, as the input 21-cm signal is brighter than the polarized foreground. The amplitude of the extracted 21-cm profile, however, has an amplitude bias at the ∼20–30 per cent level that changes with the polarization orientation that is, again, qualitatively comparable with the difference shown by Bowman et al. (2018a) when the two polarizations are rotated by 90°. A polarized contamination, enhancing the reconstructed signal, could mitigate the need to explain the anomalously high amplitude in term of exotic physics.

ACKNOWLEDGEMENTS

MS thanks Junaid Townsend for providing the SIMFAST21 outputs. MS and MGS are supported by the South African Square Kilometre Array Project and National Research Foundation. MS and GB acknowledge funding from the INAF PRIN-SKA 2017 project 1.05.01.88.04 (FORECaST). We acknowledge the support from the Ministero degli Affari Esteri della Cooperazione Internazionale – Direzione Generale per la Promozione del Sistema Paese Progetto di Grande Rilevanza ZA18GR02 and the National Research Foundation of South Africa (grant number 113121) as part of the ISARP RADIOSKY2020 Joint Research Scheme. GB acknowledges the Rhodes University research office and support from the Royal Society and the Newton Fund under grant NA150184. This work is based on research supported in part by the National Research Foundation of South Africa (grant number 103424).

REFERENCES

Barkana R., 2018, Nature, 555, 71
Bernardi G. et al., 2009, A&A, 500, 965
Bernardi G. et al., 2010, A&A, 522, A67
Bernardi G. et al., 2013, ApJ, 771, 105
Bernardi G., McQuinn M., Greenhill L. J., 2015, ApJ, 799, 90
Bernardi G. et al., 2016, MNRAS, 461, 2847
Bowman J. D., Rogers A. E. E., 2010, Nature, 468, 796
Bowman J. D., Rogers A. E. E., Monsalve R., Mozdzen T., Mahesh N., 2018a, Nature, 555, 67
Bowman J. D., Rogers A. E. E., Monsalve R. A., Mozdzen T. J., Mahesh N., 2018b, Nature, 564, E35
Brentjens M. A., de Bruyn A. G., 2005, A&A, 441, 1217
Buchner J. et al., 2014, A&A, 564, A125
Burn B. J., 1966, MNRAS, 133, 67
Cohen A., Fialkov A., Barkana R., 2016, MNRAS, 459, L90
Cohen A., Fialkov A., Barkana R., Lotem M., 2017, MNRAS, 472, 1915
DeBoer D. R. et al., 2017, PASP, 129, 045001
Dowell J., 2011, Parametric Model for the LWA-1 Dipole Response as a Function of Frequency. Long Wavelength Array (LWA) Memo #178
Ellingson S. W., Craig J., Dowell J., Taylor G. B., Helmboldt J. F., 2013, preprint (arXiv:1307.0697)
Ewall-Wice A., Chang T.-C., Lazio J., Doré O., Seiffert M., Monsalve R. A., 2018, ApJ, 868, 63
Feng C., Holder G., 2018, ApJ, 858, L17
Feroz F., Hobson M. P., 2008, MNRAS, 384, 449
Feroz F., Hobson M. P., Bridges M., 2009, MNRAS, 398, 1601
Fialkov A., Loeb A., 2013, J. Cosmol. Astropart. Phys., 11, 066
Field G. B., 1958, Proc. IRE, 46, 240
Fraser S. et al., 2018, Phys. Lett. B, 785, 159
Furlanetto S. R., Oh S. P., Briggs F. H., 2006, Phys. Rep., 433, 181
Harker G. J. A., Pritchard J. R., Burns J. O., Bowman J. D., 2012, MNRAS, 419, 1070
Harker G. J. A., Mirocha J., Burns J. O., Pritchard J. R., 2016, MNRAS, 455, 3829
Haverkorn M., Katgert P., de Bruyn A. G., 2004, A&A, 427, 549
Hills R., Kulkarni G., Meerburg P. D., Puchwein E., 2018, Nature, 564, E32
Houston N., Li C., Li T., Yang Q., Zhang X., 2018, Phys. Rev. Lett., 121, 111301
Jelić V., Zaroubi S., Labropoulos P., Bernardi G., De Bruyn A. G., Koopmans L. V. E., 2010, MNRAS, 409, 1647
Koopmans L. et al., 2015, Proceedings of Advancing Astrophysics with the Square Kilometre Array (AASKA14). Available at: http://pos.sissa.it/cgi-bin/reader/conf.cgi?confid=215
Lenc E. et al., 2016, ApJ, 830, 38
Madau P., Meiksin A., Rees M. J., 1997, ApJ, 475, 429
Martinot Z. E., Aguirre J. E., Kohn S. A., Washington I. Q., 2018, ApJ, 869, 79
Mesinger A., Ferrara A., Spiegel D. S., 2013, MNRAS, 431, 621
Mesinger A., Greig B., Sobacchi E., 2016, MNRAS, 459, 2342
Mirocha J., 2014, MNRAS, 443, 1211
Mirocha J., Harker G. J. A., Burns J. O., 2015, ApJ, 813, 11
Mirocha J., Furlanetto S. R., Sun G., 2017, MNRAS, 464, 1365
Monsalve R. A., Rogers A. E. E., Bowman J. D., Mozdzen T. J., 2017, ApJ, 847, 64
Monsalve R. A., Greig B., Bowman J. D., Mesinger A., Rogers A. E. E., Mozdzen T. J., Kern N. S., Mahesh N., 2018, ApJ, 863, 11
Monsalve R. A., Fialkov A., Bowman J. D., Rogers A. E. E., Mozdzen T. J., Cohen A., Barkana R., Mahesh N., 2019, ApJ, 875, 67
Moore D. F., Aguirre J. E., Parsons A. R., Jacobs D. C., Pober J. C., 2013, ApJ, 769, 154
Mozdzen T. J., Bowman J. D., Monsalve R. A., Rogers A. E. E., 2016, MNRAS, 455, 3890
Nhan B. D., Bradley R. F., Burns J. O., 2017, ApJ, 836, 90
Nunhokee C. D. et al., 2017, ApJ, 848, 47
Ord S. M. et al., 2010, PASP, 122, 1353
Philip L. et al., 2019, J. Astron. Instrum., 8, 1950004
Planck Collaboration XIII, 2016, A&A, 594, A13
Presley M. E., Liu A., Parsons A. R., 2015, ApJ, 809, 18
Price D. C. et al., 2018, MNRAS, 478, 4193
Pritchard J. R., Furlanetto S. R., 2007, MNRAS, 376, 1680
Pritchard J., Loeb A., 2010, Nature, 468, 772
Santos M. G., Ferramacho L., Silva M. B., Amblard A., Cooray A., 2010, MNRAS, 406, 2421
Sathyanarayana Rao M., Subrahmanyan R., Udaya Shankar N., Chluba J., 2017, AJ, 153, 26
Sharma P., 2018, MNRAS, 481, L6
Shaver P. A., Windhorst R. A., Madau P., de Bruyn A. G., 1999, A&A, 345, 380
Singh S., Subrahmanyan R., 2019, ApJ, 880, 26
Singh S. et al., 2017, ApJ, 845, L12
Singh S., Subrahmanyan R., Shankar N. U., Rao M. S., Girish B. S., Raghunathan A., Somashekar R., Srivani K. S., 2018, Exp. Astron., 45, 269
Spinelli M., Bernardi G., Santos M. G., 2018, MNRAS, 479, 275 (S18)
Switzer E. R., Liu A., 2014, ApJ, 793, 102
Tauscher K., Rapetti D., Burns J. O., Switzer E., 2018, ApJ, 853, 187
Taylor G. B. et al., 2012, J. Astron. Instrum., 1, 1250004
Tribble P. C., 1992, MNRAS, 256, 281
Venkatesan A., Giroux M. L., Shull J. M., 2001, ApJ, 563, 1
Voytek T. C., Natarajan A., Jáuregui García J. M., Peterson J. B., López-Cruz O., 2014, ApJ, 782, L9
Wouthuysen S. A., 1952, AJ, 57, 31
Zwart J. T. L., Price D., Bernardi G., 2016, Astrophysics Source Code Library, record ascl:1606.004

This paper has been typeset from a TEX/LATEX file prepared by the author.